

1 A deep learning-based dual latent space method for the  
2 estimation of physical flow properties from fiber-optic  
3 measurements

4 Misael M. Morales<sup>1\*</sup>, Alberto Mendoza<sup>2</sup>, Martin Sundin<sup>2</sup>, Cagri Cerrahoglu<sup>2</sup>, Michael J.  
5 Pyrcz<sup>1,3</sup>, and Carlos Torres-Verdín<sup>1,3</sup>

6 1. Hildebrand Department of Petroleum and Geosystems Engineering, The University of Texas at Austin

7 2. Lytt Limited

8 3. Jackson School of Geosciences, The University of Texas at Austin

9 \*Corresponding author; email: [misaelmorales@utexas.edu](mailto:misaelmorales@utexas.edu)

10 **Abstract**

11 Distributed fiber optic sensing (DFOS) technologies have emerged as cost-effective high-resolution monitoring  
12 alternatives over conventional geophysical techniques. However, due to the large volume and noisy nature  
13 of the measurements, significant processing is required and expert, fit-for-purpose tools must be designed to  
14 interpret and utilize DFOS measurements. Deep learning techniques provide the flexibility and efficiency to  
15 process and utilize DFOS measurements to estimate subsurface energy resource properties. We propose a  
16 deep learning-based dual latent space method to process distributed acoustic sensing (DAS) and distributed  
17 temperature sensing (DTS) measurements and estimate the injection point location and relative multiphase  
18 flow rates along a flow-loop equipped with a DFOS unit. The dual latent space method is composed of  
19 two identical convolutional U-Net AutoEncoders to compress and reconstruct the DAS and DTS data,  
20 respectively. The AutoEncoders are capable of determining an optimal latent representation of the DAS  
21 and DTS measurements, which are then combined and used to estimate the physical flow properties along  
22 six different experimental trials. The predictions are obtained within 7 milliseconds and with over 99.98%  
23 similarity and less than  $3.68 \times 10^{-9}$  relative error. The method is also shown to be robust to noise, and can  
24 be applied to different multiphase scenarios with a single pre-training procedure. The proposed method is  
25 therefore capable of fast and accurate estimation of physical flow properties, and can be used for real-time  
26 monitoring in different subsurface energy resource applications.

27 **Keywords:** Distributed fiber optic sensing, Flow properties estimation, Convolutional neural network,  
28 Latent space modeling.

## 29 1 Introduction

30 Distributed fiber optic sensing (DFOS) technology offers high-resolution measurements in harsh environments  
31 where conventional electric sensors fail or are insufficient to provide detailed characterization of the  
32 environment [1, 2]. DFOS units operate by laser pulses along a fiber that interacts with imperfections in  
33 the glass and are back-scattered to the source and recorded by an interrogator [3]. DFOS units serve as a  
34 possible solution for reliable, cost-effective, and detailed monitoring of complex flow systems [4, 5]. However,  
35 though promising, this technique requires technological advances in processing and integration for useful  
36 interpretation, monitoring, and prediction in subsurface energy systems.

37 Over the last decade, DFOS systems have gained attention and popularity in the energy resource industry  
38 [6–9]. DFOS systems have also become increasingly available, reliable, and economical, resulting in their  
39 broader adoption for a wide range of subsurface applications. The two main measurements in subsurface  
40 energy resource applications are distributed acoustic sensing (DAS) and distributed temperature sensing  
41 (DTS). DAS consists of continuous measurements of axial strain rate along the fiber using Rayleigh scattering  
42 interferometry. On the other hand, DTS consists of continuous measurements of the temperature profile along  
43 the length of the fiber using the Raman effect. Moreover, DAS and DTS measurements can be realized over  
44 large distances by analyzing back-scattered signal frequency, intensity, and phase [10]. However, such high-  
45 density spatiotemporal measurements can amount to several Terabytes of data, making them challenging to  
46 process and analyze using standard techniques.

47 Machine learning (ML) techniques have emerged as candidate solutions to rapidly and efficiently process  
48 and analyze DFOS measurements [11? , 12]. Due to the recent increase in computing power and storage  
49 capacity available, ML techniques provide a significant advantage for understanding DFOS measurements.  
50 More specifically, deep learning (DL) techniques based on neural network models have proven capable and  
51 flexible to process DFOS measurements efficiently and provide accurate predictions of subsurface properties  
52 [13, 14]. On the other hand, latent space modeling techniques have proven useful to extract salient information  
53 from large datasets, providing a reduced-dimensionality representation of the features and accelerating  
54 the processing workflow [15, 16].

55 Several attempts have been made in ML-based and DL-based techniques for DFOS processing and analysis  
56 in the energy resources industry [17–19]. Bhattacharya et al. [20] were the first to compare different ML  
57 techniques to predict hydrocarbon production from multiple data sources, including DFOS measurements.  
58 They use DAS and DTS data to evaluate the well performance over time for a multi-stage stimulated gas  
59 well in the Marcellus Shale. They show that different ML techniques are efficient and accurate in predicting  
60 daily gas production compared to traditional highly-complex simulations, and that DFOS measurements

61 are sufficiently high in spatial and temporal resolution to provide accurate predictions of well performance.  
62 However, their methodology focuses on incorporating pre-processed multi-source, multi-physics data to aid  
63 a single prediction, rather than focusing on real-time processing of high-resolution DAS and DTS.

64 The application of DL-based techniques for subsurface monitoring and characterization using DFOS  
65 measurements has also been widely explored [21, 22]. Sherman et al. [13] developed a physics-informed neural  
66 network (PINN) to predict the physical properties of a hydraulic fracture from DAS measurements. Their  
67 method consists of a three-part neural network: (1) a convolutional neural network (CNN) to parameterize  
68 the DAS measurements, (2) an artificial neural network (ANN) to parameterize geometric factors such as  $x$   
69 and  $y$  locations, and (3) a second ANN to merge the two previous parameterizations and predict the hydraulic  
70 fracture physical properties such as height and length. It is important to note that they pre-process the DAS  
71 measurements and rescale and resample them into conformable units for the DL model. Moreover, their work  
72 does not incorporate a spatial component for dynamic monitoring. Huot et al. [23] developed a DL-based  
73 method for detection and characterization of microseismic events from DAS measurements. Their model  
74 consists of a convolutional neural network to process DAS measurements and reconstruct the corresponding  
75 microseismic response. They show that DAS measurements can be used as a replacement to expensive and  
76 complex seismic surveys to provide high-resolution subsurface monitoring.

77 We propose a deep learning-based dual latent space model to estimate the physical flow properties of a  
78 subsurface energy resource system from DFOS measurements. The dual latent space model is based on two  
79 mirrored convolutional U-net AutoEncoders to compress and reconstruct the DAS and DTS measurements,  
80 and a latent regression function to estimate the injection point location and relative multiphase flow rates at  
81 each injection point. The method is tested using DFOS measurements from a flow-loop experiment consisting  
82 of different trials with multiphase flow of oil, gas, water, and sand. Furthermore, we compare the efficiency  
83 and accuracy of the method using the dual latent space model as opposed to a single latent space model,  
84 and quantify the uncertainty in the estimation based on different levels of noise in the DFOS measurements.

85 Section 2 describes the design of the flow-loop experiments, data processing, and the architecture of  
86 the dual latent space model. Section 3 shows the results for 6 different trials, as well as a comparison  
87 against a single latent space model, and the uncertainty quantification for the flow parameter estimation.  
88 Finally, Section 4 provides the conclusions, challenges, and future research opportunities for deep learning  
89 applications in DFOS analysis.

90 **2 Methodology**

91 This section describes the design of the flow-loop experiments, the DFOS data processing, and the architec-  
 92 ture of the dual latent space model.

93 **2.1 Flow-loop Experiment Design**

94 Given that supervised ML and DL models require labeled data for training, we rely on laboratory results from  
 95 numerous flow-loop experiments. The flow-loop is designed with a specified distance between the injection  
 96 points, and variable multiphase flow characteristics for background and injection points flow, namely the  
 97 physical flow properties. A fiber optic cable is placed between the tubing and the casing to continuously  
 98 record DAS and DTS measurements. Figure 1 shows a simplified diagram of the flow-loop design, adapted  
 99 from [24].

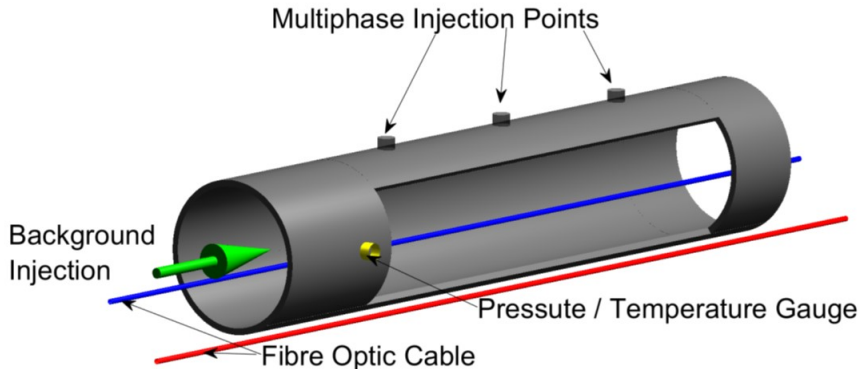


**Figure 1:** Schematic of multiphase flow-loop with DFOS unit for experimental data acquisition (for more experimental details see [25]).

100 The experiments are composed of 6 trials, where the background and injection point flow vary in terms  
 101 of rate and phases. Table 1 summarize the 6 experimental trials. Similarly, Figure 2 shows a graphical  
 102 representation of the multiphase flow rates for each trial, and their normalized values. Normalization is  
 103 applied using *MinMax* scaling, such that:

$$\hat{x} = \frac{x - \min(x)}{\max(x) - \min(x)}, \quad (1)$$

104 where  $x$  represents the original data, and  $\hat{x}$  is the normalized data. The normalized data therefore lies in  
 105 the range of  $[0, 1]$ . This is done to aid the deep learning nonlinear activation functions and backpropagation  
 106 stability, and to obtain representative error metrics during the training process.

**Table 1:** Summary of multiphase flow rates for each of the 6 trials in the flow-loop experiments, expressed in the following units: oil (bpd), gas (cfd), water (bpd), sand (pptb).

	Trial 45				Trial 48			
	Oil	Gas	Water	Sand	Oil	Gas	Water	Sand
Background	1500	0	0	0	3000	0	0	0
Injection 1	250	8250	0	0	500	0	0	0
Injection 2	250	8250	0	0	150	0	1500	0
Injection 3	0	0	0	0	100	0	0	0
Injection 4	0	0	0	0	5000	0	0	0
	Trial 54				Trial 64			
	Oil	Gas	Water	Sand	Oil	Gas	Water	Sand
Background	1500	50000	0	0	3000	100000	0	0
Injection 1	250	8333.33	1000	0	250	8333.33	250	0
Injection 2	250	8333.33	0	0	250	8333.33	100	0
Injection 3	0	0	0	0	0	0	0	0
Injection 4	500	16666.66	1000	0	250	8333.33	250	0
	Trial 109				Trial 128			
	Oil	Gas	Water	Sand	Oil	Gas	Water	Sand
Background	6000	90000	0	0	3000	60000	0	0
Injection 1	500	7500	0	0	500	20000	0	0
Injection 2	500	7500	0	0	500	20000	0	0
Injection 3	0	0	0	0	0	0	0	0
Injection 4	0	0	500	10	500	20000	0	5

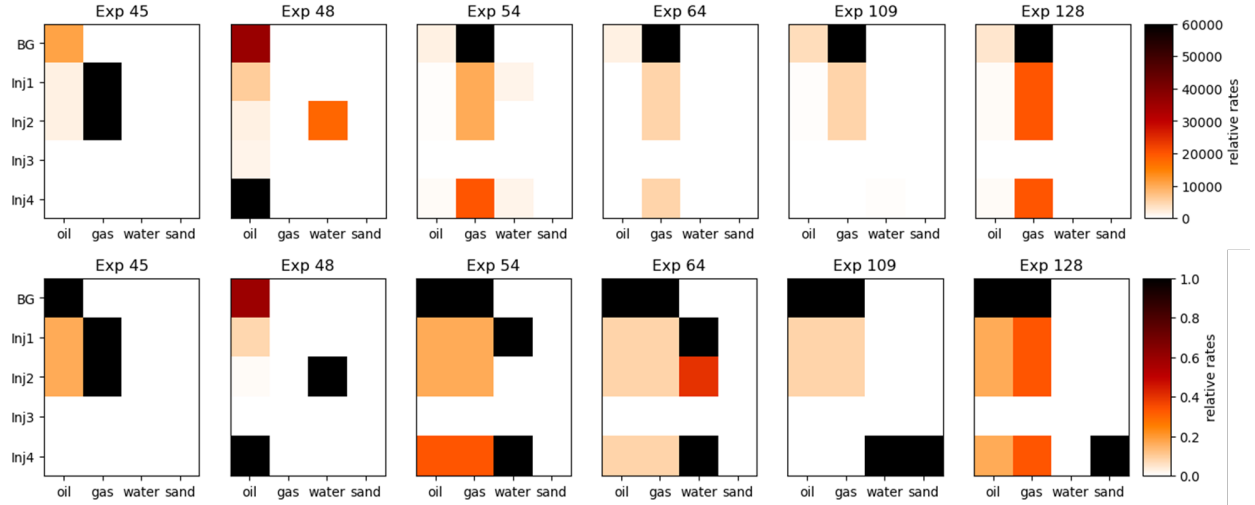


**Figure 2:** Visual representation of the multiphase flow rates for each of the 6 trials in the flow-loop experiments. The top row shows the multiphase flow rates in their original units, and the bottom row shows the normalized flow rates.

## 107 2.2 Data Processing

108 The DAS and DTS measurements for each experimental trial consists of approximately 100 Gb of data.  
 109 Therefore, significant data processing is required to crop and rescale the DAS and DTS measurements into  
 110 manageable sizes that retain all the significant information.

111 During the experiments, the fiber optic cable has a total length of 5,504 meters. This is done to represent  
 112 the approximate depth of a well. However, the majority of this cable is unused since the flow-loop only has  
 113 approximately under 200 meters in length. Thus, we crop the data to a 200-meter window around the flow-  
 114 loop. This significantly reduces the dimensionality of the data and allows for more manageable processing  
 115 and inference. Furthermore, we match the injection point locations to their corresponding distance along the  
 116 flow-loop to make a sparse representation of the injection point location and relative multiphase flow rate  
 117 for each trial. Figure 3 shows the relative multiphase flow rates for each of the 6 trials within the significant  
 118 window of the flow-loop.

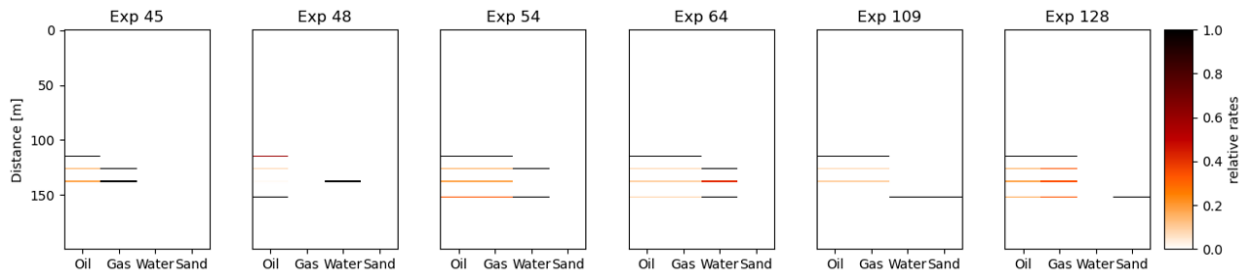


**Figure 3:** Relative multiphase flow rate and injection point location for each of the 6 trials in the experiment.

119     Each experimental trial is run for a slightly different time length, resulting in measurement data of differ-  
 120    ent sizes. Moreover, the DAS and DTS interrogators record temporal measurements at different frequencies,  
 121    also resulting in measurement data of different sizes. For example, Trial 1 has approximately 108,000  
 122    DAS temporal measurements and 78 DTS temporal measurements, and Trial 6 approximately 126,000 DAS  
 123    temporal measurements and 93 DTS temporal measurements. These invalidate the requirements for training  
 124    deep learning models, where each sample must have the same dimensions as the others in terms of spatial and  
 125    temporal coordinates. To tackle this, we apply a smart sampling strategy using Latin Hypercube Sampling  
 126    (LHS) [26].

127     Let  $d_A$  represent the DAS data for a given experimental trial, and  $d_T$  represent the DTS data. The  
 128    dimensions of  $d_A$  and  $d_T$  are given by  $(m_A, n_A)$  and  $(m_T, n_T)$ , respectively. Let  $m$  represent the spatial  
 129    dimension, and  $n$  represent the temporal dimension. Recall that we crop the spatial dimension to a 200-  
 130    meter window centered along the flow-loop. Thus,  $m_A = m_T = 200$ . To normalize the temporal coordinates,  
 131    we resample the DAS measurements to the same frequency as the DTS measurements using LHS. This  
 132    allows for representative sampling of the DAS signal at the same frequency as the DTS signal, without  
 133    decimating or aliasing the DAS measurements. Now, for each trial in the experiment,  $n_A = n_T = n$ , where  
 134     $n$  can vary between experiments. Figure 4 shows the processed, resampled, and normalized DAS and DTS  
 135    measurements for two sample trials in the experiment.

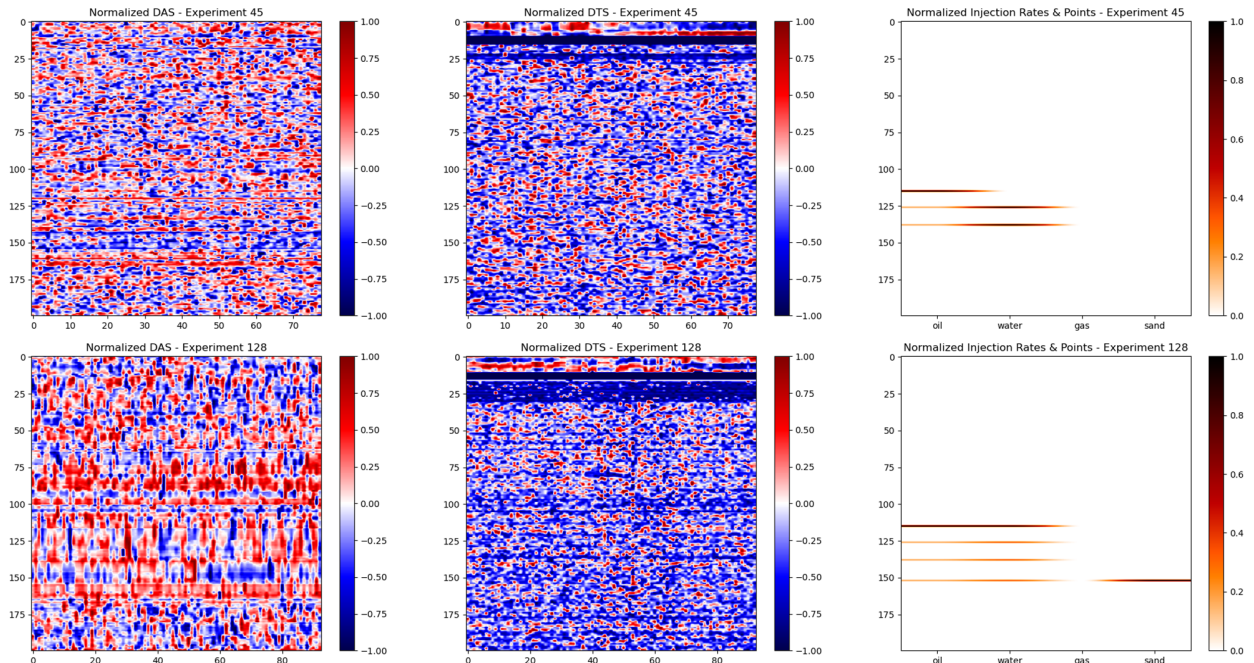


**Figure 4:** Visualization of the DAS (left), DTS (center) and physical flow properties (right) for two trials in the experiment. The top row shows Experiment 45, and the bottom row shows Experiment 128.

## <sup>136</sup> 2.3 Model Architecture

<sup>137</sup> AutoEncoders (AE) are a type of semi-supervised deep learning architecture that compress, or encode, the  
<sup>138</sup> original data,  $X$ , into a latent representation  $z$ , and then use a mirror architecture of the encoder, called  
<sup>139</sup> a decoder, to reconstruct the data into  $\hat{X}$ . Figure 5 shows a simple representation of an AE architecture.  
<sup>140</sup> The goal is to minimize the differences between  $X$  and  $\hat{X}$  by optimizing the parameters within the Encoder  
<sup>141</sup> ( $Enc$ ) and Decoder ( $Dec$ ) portions of the network. AEs can be expressed as follows:

$$\hat{X} = Dec(Enc(X)) = Dec(z) \quad (2)$$

<sup>142</sup> such that  $\min(\hat{e})$ , where  $\hat{e} = \|X - \hat{X}\|$ . A perfect AE will result in loss-less compression of the data  $X$ ,  
<sup>143</sup> such that  $\hat{X} \equiv X$ . However, in practice, we will always obtain a lossy compression of  $X$ , such that  $\hat{X} \approx X$ .  
<sup>144</sup> This is not necessarily bad, since the latent representation,  $z$ , might contain sufficient information about  $X$   
<sup>145</sup> to estimate or predict our quantity of interest (e.g., physical flow properties) when  $X$  is excessively large.

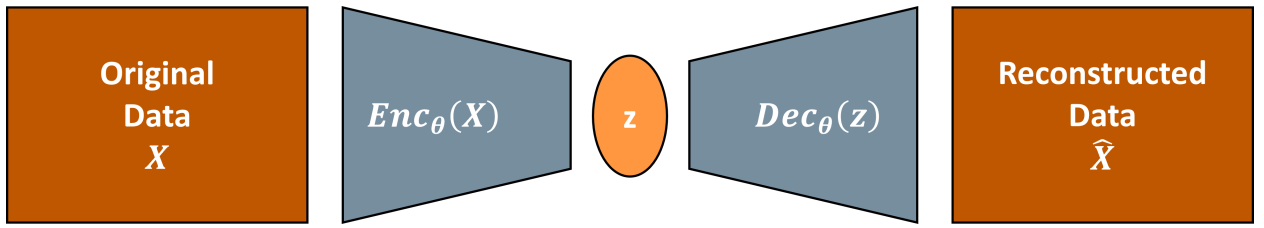


**Figure 5:** Simplified schematic of an AutoEncoder model. The original data,  $X$ , is encoded into a latent representation,  $z$ , and then decoded using a mirror image of the encoder to reconstruct the data,  $\hat{X}$ .

<sup>146</sup> A convolutional U-Net AutoEncoder [27], is a specific AE architecture where the hidden layers consist of  
<sup>147</sup> convolutions and residual concatenations at each hidden layer between the mirrored Encoder and Decoder  
<sup>148</sup> portions. Figure 6 shows a simplified schematic of a convolutional U-Net AutoEncoder architecture.

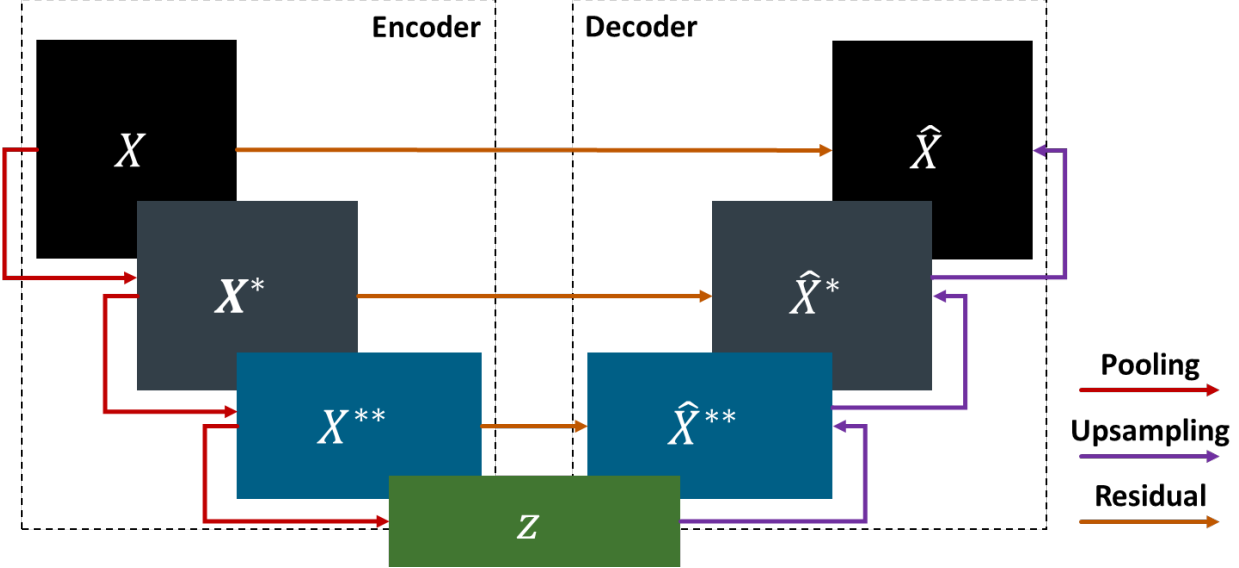


**Figure 6:** Schematic of a convolutional U-Net AutoEncoder architecture. The original data,  $X$ , is encoded into a latent representation,  $z$ , and a mirror Decoder reconstructs the original data into  $\hat{X}$ . Residual concatenations connect each mirrored hidden layer between the Encoder and Decoder portions of the network.

149     Each convolutional U-Net AutoEncoder is composed of four encoding layers and four mirroring decoding  
 150    layers. In each encoding layer we perform two repeated padded convolutions and batch normalization, with  
 151    a LeakyReLU activation function and a max pooling. On the other hand, each decoding layer is composed  
 152    of a transposed convolution followed by a residual concatenation and two repeated padded convolutions and  
 153    batch normalization with LeakyReLU activation. Figure 7 shows the detailed schematic of each encoding  
 154    and decoding layer.

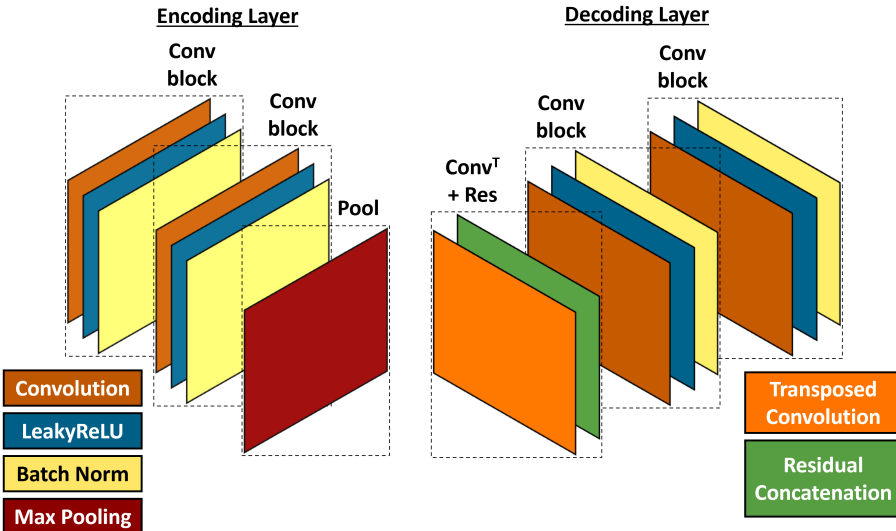


**Figure 7:** Detailed schematic of each encoding (left) and decoding (right) layer in the convolutional U-Net AutoEncoder architecture.

155 Our proposed dual latent space method merges two convolutional U-Net AutoEncoders into a single  
 156 framework. The first AE compresses and reconstructs the DAS measurements, and the second AE compresses  
 157 and reconstructs the DTS measurements. Both AEs are identical to each other, but trained separately to  
 158 capture the distinct features that are intrinsic to each separate data source. We pre-train each AE to  
 159 optimally compress and reconstruct the DAS and DTS measurements, respectively. This ensures that the  
 160 latent representations obtained from each AE will optimally represent the DAS and DTS data, respectively.  
 161 This procedure can be expressed as follows:

$$z_i = Enc_{\theta_i}(X_i), \quad (3)$$

162

$$\hat{X}_i = Dec_{\psi_i}(Enc_{\theta_i}(X_i)) = Dec_{\psi_i}(z_i), \quad (4)$$

163 where  $i = \{DAS, DTS\}$ , and  $\theta_i$  and  $\psi_i$  are the Encoder and Decoder loss for the DAS and DTS AEs,  
 164 respectively.

165 We extract only the Encoder portions of each AE and use the obtained latent representations,  $z_i$ , to  
 166 construct a dual latent space, namely  $z^*$ , from the concatenation of the DAS and DTS latent spaces such  
 167 that  $z^* = [z_{DAS}, z_{DTS}]$ . The physical flow properties,  $y$ , are then estimated using a latent regressor,  $f$ , such  
 168 that  $y = f(z^*)$ . Figure 8 shows the architecture to estimate the physical flow properties from the dual latent  
 169 space using the pre-trained DAS and DTS Encoders only. Figure 9 shows the complete architecture for our  
 170 dual latent space method.

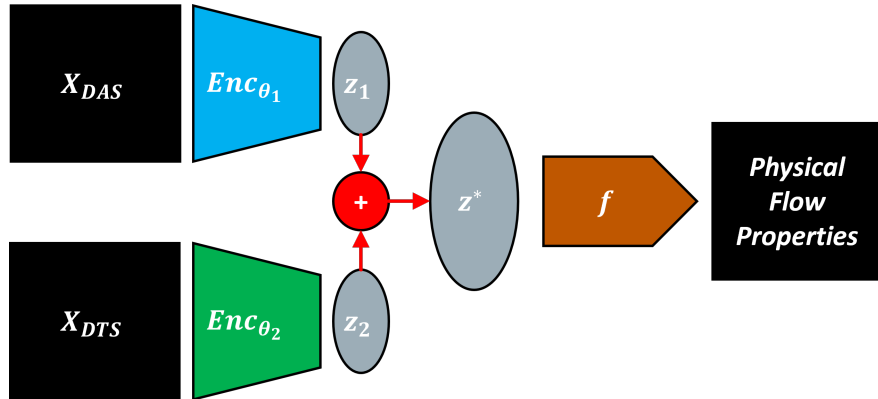


**Figure 8:** Schematic of the dual latent space method to estimate physical flow properties from DAS and DTS measurements. The pre-trained DAS (blue) and DTS (green) encoders are used to generate their corresponding latent spaces, which are combined into  $z^*$  and used to predict the physical flow properties,  $y$ , with a latent regressor,  $f$ .

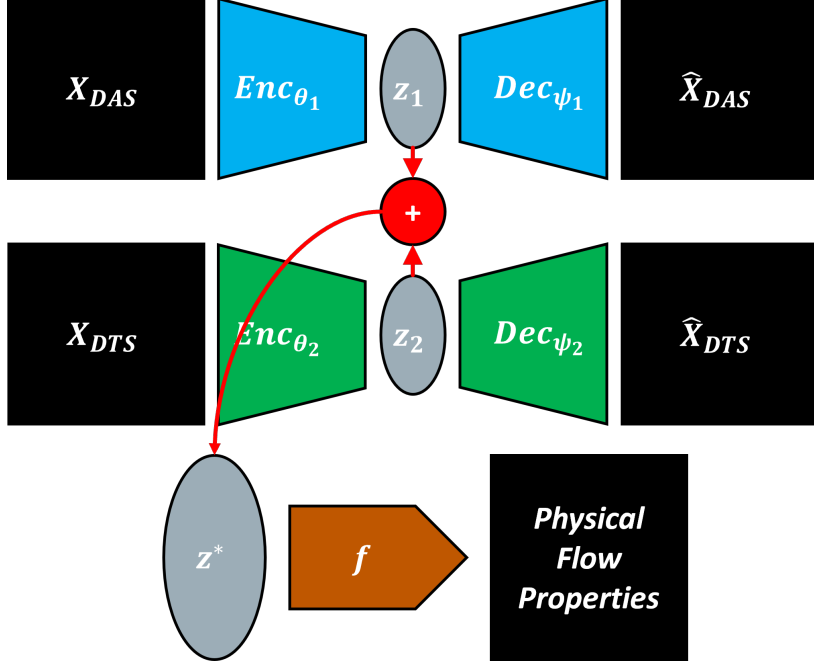


**Figure 9:** Schematic of the complete dual latent space model architecture. The DAS AE encodes  $X_{DAS}$  into  $z_1$  and decodes to reconstruct  $\hat{X}_{DAS}$  (blue). The DTS AE encodes  $X_{DTS}$  into  $z_2$  and decodes to reconstruct  $\hat{X}_{DTS}$  (green). The two latent spaces,  $z_1$  and  $z_2$ , are combined into a dual latent space,  $z^*$ , which is used to predict the physical flow properties, such that  $y = f(z^*)$ .

### 171 3 Results

172 This section describes the training performance and prediction accuracy dual latent space model, and provides  
 173 a comparison of single latent space models and uncertainty quantification in the physical flow parameter  
 174 prediction.

#### 175 3.1 Dual AutoEncoder Performance

176 The DAS and DTS AEs are trained separately using an NVIDIA RTX 3080 GPU. Each AE has a total of  
 177 45,333 parameters. We train each AE for 150 epochs with a batch size of 10, using a validation split of  
 178 20%. Only one experimental trial is used to train the AEs, and we test the performance using the other  
 179 experimental trials. The total training time required for each AE is approximately 2 minutes and 20 seconds.  
 180 We use the Adam optimizer [28] with learning rate  $1 \times 10^{-3}$ , and a Mean Squared Error (MSE) loss function.  
 181 The training and validation performance per epoch for the DAS and DTS AEs is shown in Figure 10. We  
 182 observe minimal overfit in the validation set, corresponding to good model generalizability and reconstruction  
 183 accuracy for the DAS and DTS data. The models are then capable of predicting the reconstructed DAS and  
 184 DTS measurements extremely fast and accurately. To quantify the prediction accuracy, we use the structural

185 similarity index measure (SSIM) [29], MSE, and Peak Signal-to-Noise Ratio (PSNR) of the true and predicted  
 186 physical flow properties. SSIM provides a perceptual image-to-image comparison of luminance, contrast, and  
 187 structure, while MSE provides a pixel-wise intensity comparison. In the case of DAS predictions, we obtain  
 188 an SSIM of 94.68, MSE of  $1.49 \times 10^{-2}$ , and PSNR of 24.3 dB. For DTS predictions, we obtain an SSIM  
 189 of 94.37, MSE of  $8.34 \times 10^{-3}$ , and PSNR of 26.81 dB. Figures 11 and 12 show the original DAS and DTS  
 190 measurements used for training, their reconstructions, the absolute error, and a visualization of the latent  
 191 space, respectively.

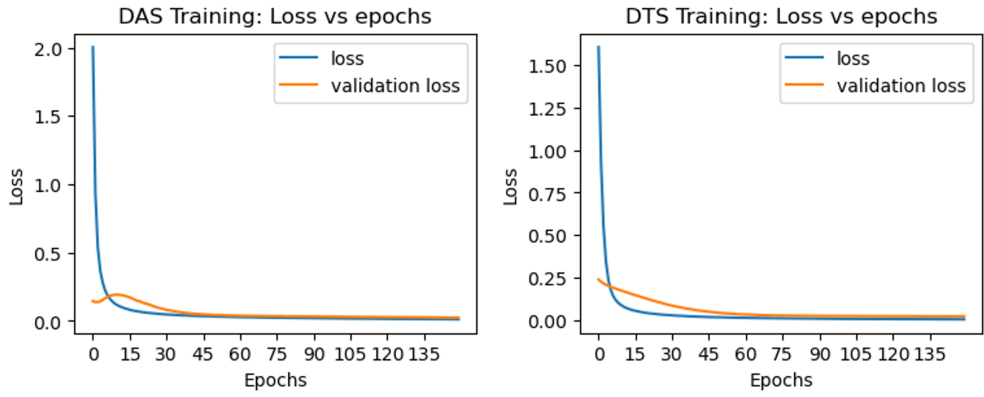


**Figure 10:** The total training and validation losses,  $\mathcal{L}$ , as a function of epoch number.

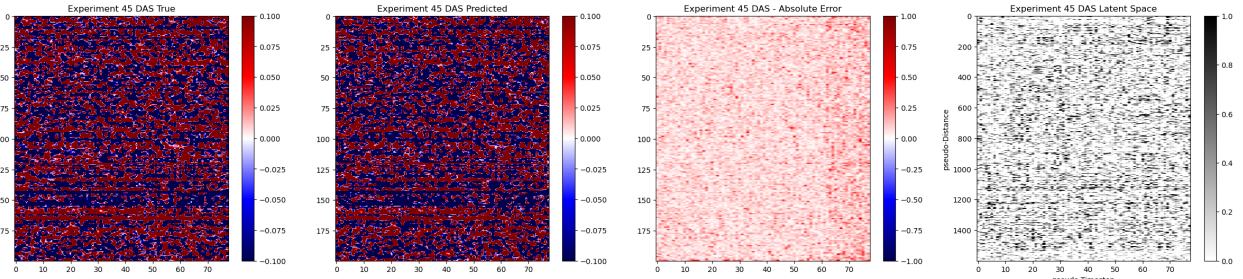


**Figure 11:** DAS AutoEncoder results for a training realization. (A) shows the normalized DAS data, (B) shows the reconstructed DAS, (C) shows the absolute error, and (D) shows a visualization of the DAS latent space for this training realization.

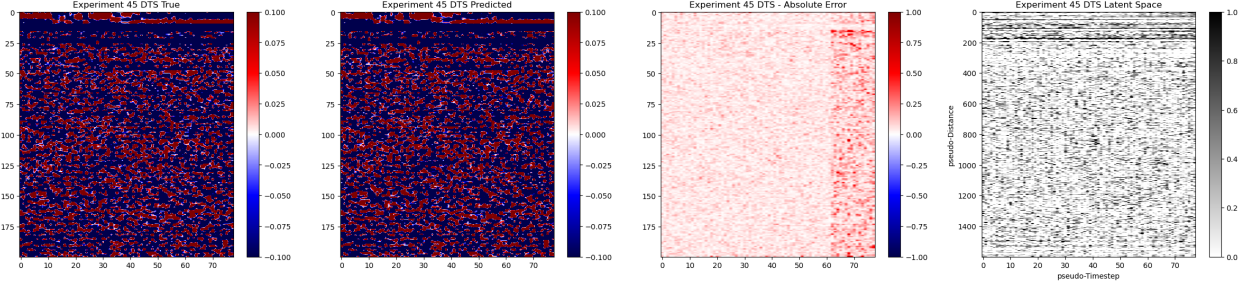


**Figure 12:** DTS AutoEncoder results for a training realization. (A) shows the normalized DTS data, (B) shows the reconstructed DTS, (C) shows the absolute error, and (D) shows a visualization of the DTS latent space for this training realization.

### 192 3.2 Flow Property Estimation

193 Once we have trained DAS and DTS AEs, we can extract the pre-trained Encoders and utilize them to  
 194 construct dual latent spaces for the other experimental trials that were not used in the training procedure.  
 195 Given that the DAS and DTS measurements have a dimensionality of approximately (200, 80), and the  
 196 physical flow properties have a dimensionality of (200, 4), the estimation of the physical flow properties  
 197 yields a highly over-determined inverse problem. Therefore, we choose to train a simple  $\ell_2$ -regularized linear  
 198 model to predict the physical flow properties from the dual latent space. This can be expressed as:

$$\hat{y} = \|f(z^*) - y\|_2^2 + \lambda\|z^*\|_2^2, \quad (5)$$

199 where  $\lambda$  is the regularization weight, defined empirically as  $\lambda = 2$ .

200 We trained the dual latent space model with data from Trial 109, given that it contains measurements  
 201 from all four phases (oil, water, gas, and sand). We then test the method with the other experimental trials.  
 202 In other words, we train the DAS and DTS AEs with data from Trial 109, and use the pre-trained Encoders  
 203 to compress the DAS and DTS measurements from the other trials and estimate the corresponding physical  
 204 flow properties. Figure 13 shows the true and predicted physical flow properties from the test trials, and  
 205 Table 2 presents the prediction accuracy metrics.

**Table 2:** Accuracy metrics for physical flow property prediction for test cases.

Trial Number	45	48	54	64	128
MSE	$3.68 \times 10^{-9}$	$3.55 \times 10^{-9}$	$2.72 \times 10^{-9}$	$3.61 \times 10^{-9}$	$3.92 \times 10^{-9}$
SSIM	99.98	99.98	99.99	99.98	99.97

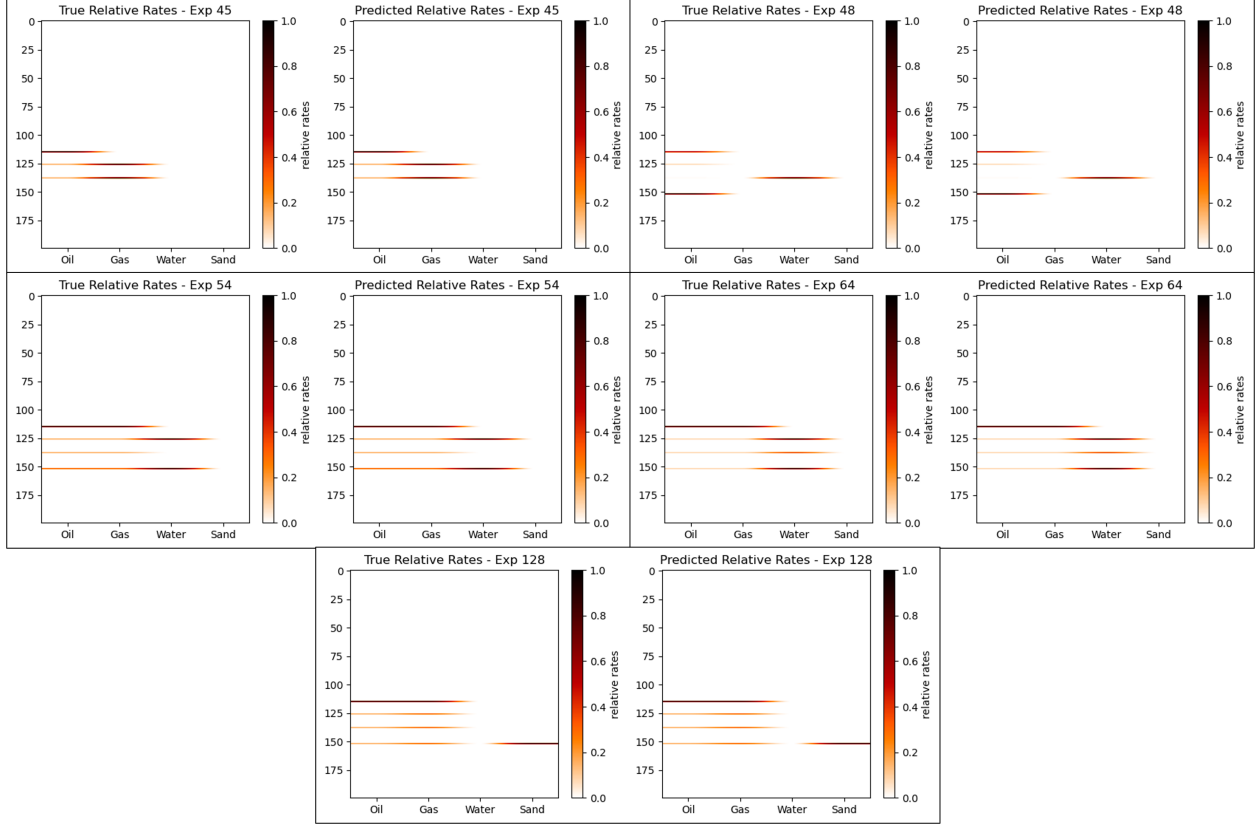


**Figure 13:** True and predicted physical flow properties for test realizations.

### 206 3.3 Dual vs. Single Latent Space

207 Given that the problem of estimating the physical flow properties from the DAS and DTS data is a highly  
 208 over-determined inverse problem, we also test the prediction performance of using a single latent space model  
 209 as opposed to our dual latent space model.

210 Using the pre-trained DAS and DTS Encoders,  $Enc_{\theta_i}$ , we construct a single latent space representation  
 211 of the DAS and DTS data, respectively, and use it to estimate the physical flow properties in each test  
 212 trial. Namely,  $\hat{y}_i = f(z_i) = f(Enc_{\theta_i}(X_i))$ , as opposed to the proposed dual latent space model case where  
 213  $\hat{y} = f(z^*) = f([Enc_{\theta_1}(X_{DAS}), Enc_{\theta_2}(X_{DTS})])$ . Figures 14, 15, and 16 compares the prediction using a  
 214 single latent space representation with DAS measurements, a single latent space representation with DTS  
 215 measurements, and the proposed dual latent space model for the test trials 45, 64, and 128, respectively.  
 216 Table 3 shows the prediction accuracy metrics for the three scenarios of all of the five test cases.

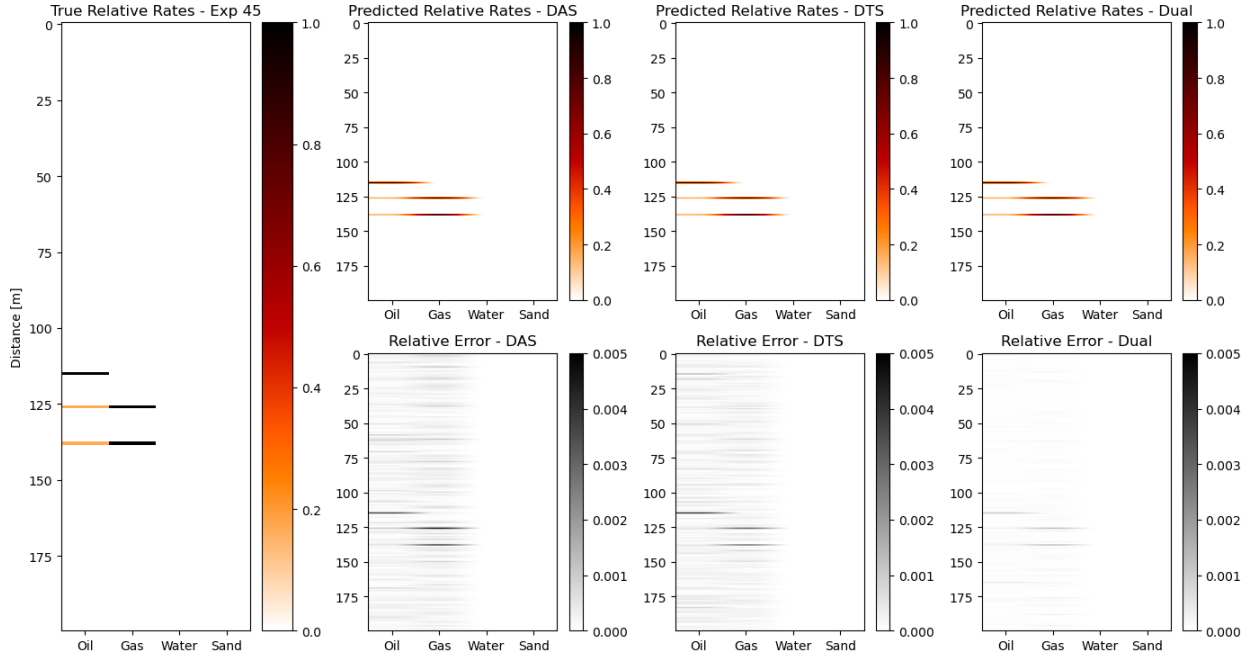


**Figure 14:** Comparison of single and dual latent space models for Trial 45; (A) is the true relative rates, (B) is the single-DAS prediction, (C) is the single-DTS prediction, and (D) is the dual latent space prediction.

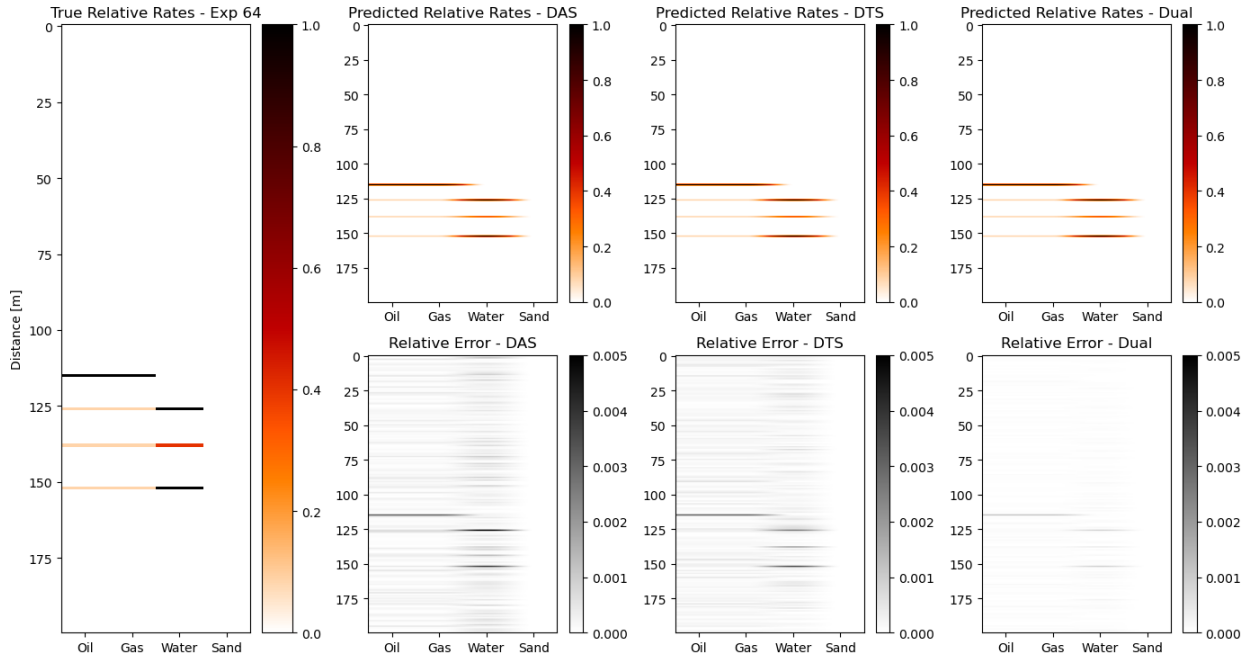


**Figure 15:** Comparison of single and dual latent space models for Trial 64; (A) is the true relative rates, (B) is the single-DAS prediction, (C) is the single-DTS prediction, and (D) is the dual latent space prediction.

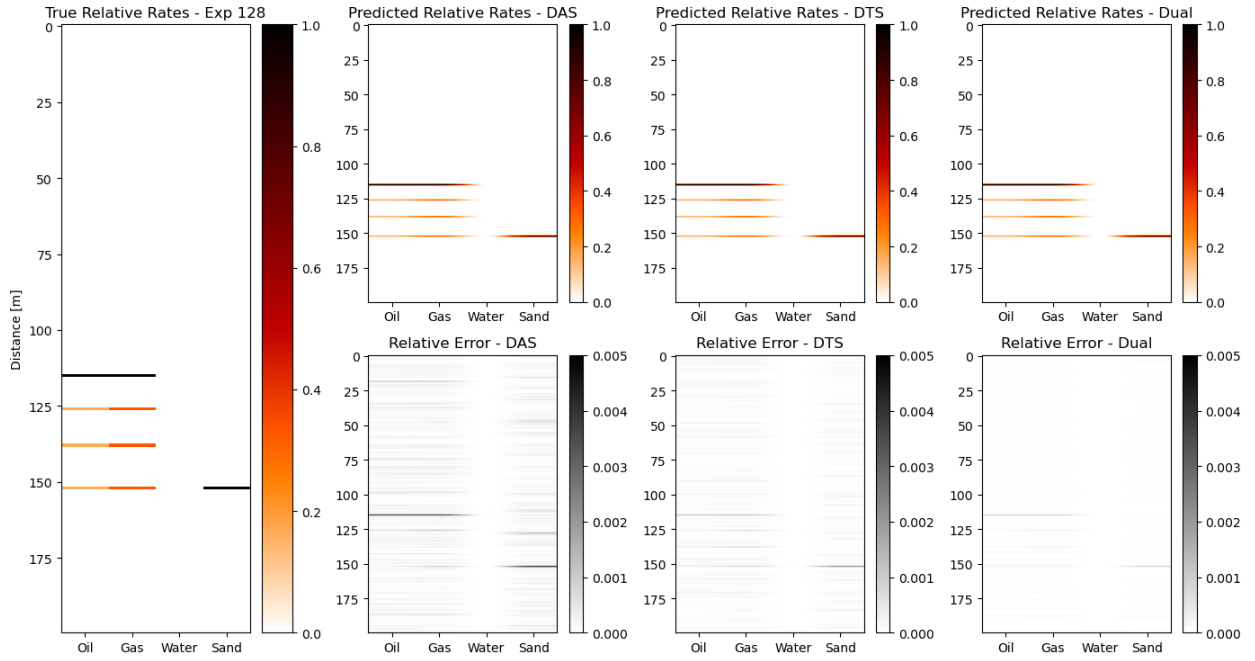


**Figure 16:** Comparison of single and dual latent space models for Trial 128; (A) is the true relative rates, (B) is the single-DAS prediction, (C) is the single-DTS prediction, and (D) is the dual latent space prediction.

**Table 3:** Prediction accuracy metrics for all test trials using single DAS latent space, single DTS latent space, and Dual latent space models.

Trial Number	Latent Representation	MSE	SSIM
45	DAS	$9.82 \times 10^{-8}$	99.95
	DTS	$6.97 \times 10^{-8}$	99.96
	Dual	$3.68 \times 10^{-9}$	99.98
48	DAS	$7.93 \times 10^{-8}$	99.96
	DTS	$4.41 \times 10^{-8}$	99.97
	Dual	$3.55 \times 10^{-9}$	99.98
54	DAS	$8.20 \times 10^{-8}$	99.96
	DTS	$2.52 \times 10^{-8}$	99.97
	Dual	$2.72 \times 10^{-9}$	99.99
64	DAS	$1.29 \times 10^{-7}$	99.93
	DTS	$8.29 \times 10^{-8}$	99.95
	Dual	$3.61 \times 10^{-9}$	99.98
128	DAS	$7.04 \times 10^{-8}$	99.95
	DTS	$1.52 \times 10^{-8}$	99.96
	Dual	$3.92 \times 10^{-9}$	99.97

### 217 3.4 Uncertainty Quantification

218 Naturally, DAS and DTS measurements are very noisy in nature due to the subsurface and operational  
 219 conditions. Therefore, we decide to quantify the uncertainty in our physical flow property predictions by  
 220 adding different levels of random noise to the DAS and DTS data in our dual latent space model. Let  $\varepsilon$  be  
 221 the random noise, such that  $\varepsilon \sim \mathcal{N}(0, \sigma_i)$ , where  $\sigma_i$  is the standard deviation of the original DAS or DTS  
 222 data,  $X_i$ . The noisy DAS and DTS measurements are given by  $\tilde{X}_i = X + p * \varepsilon$ , where  $p$  is the percent  
 223 noise added. We quantify the uncertainty with in our predictions with 5%, 10%, 25%, and 50% added noise.  
 224 Figures 17, 18, and 19 show the results in estimating physical flow properties by of adding different levels of  
 225 noise to the dual latent space model.

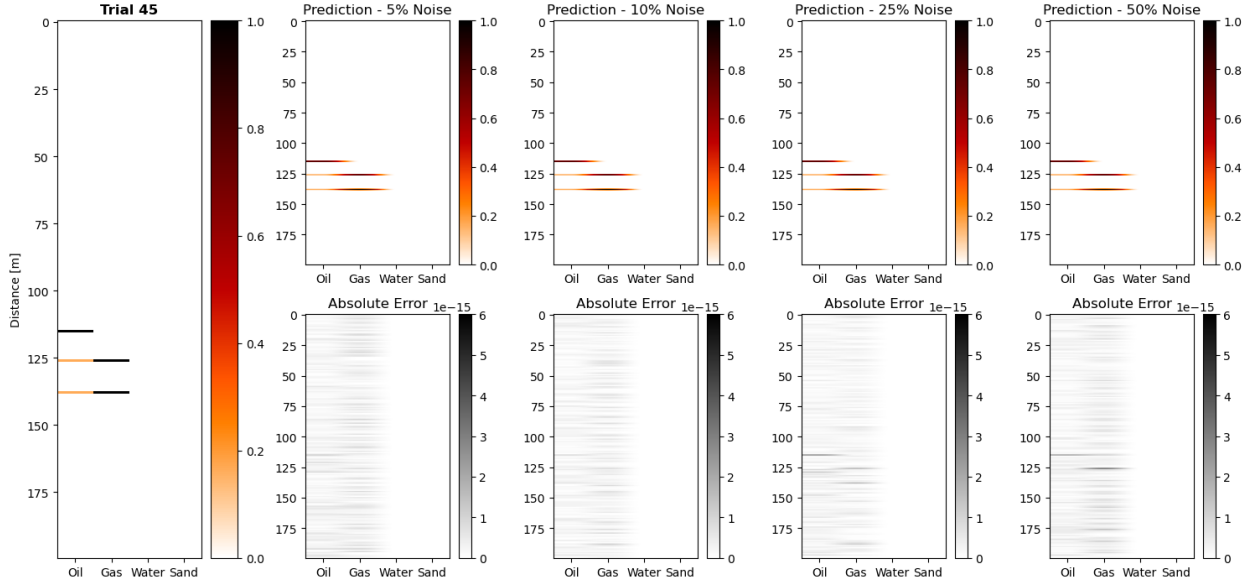


**Figure 17:** Prediction of physical flow properties for Trial 45 with different levels of added noise; (A) is the true relative rates, (B) 5% noise, (C) 10% noise, (D) 25% noise, and (E) 50% noise. The top row shows the estimated physical flow properties, and the bottom row shows the absolute error.

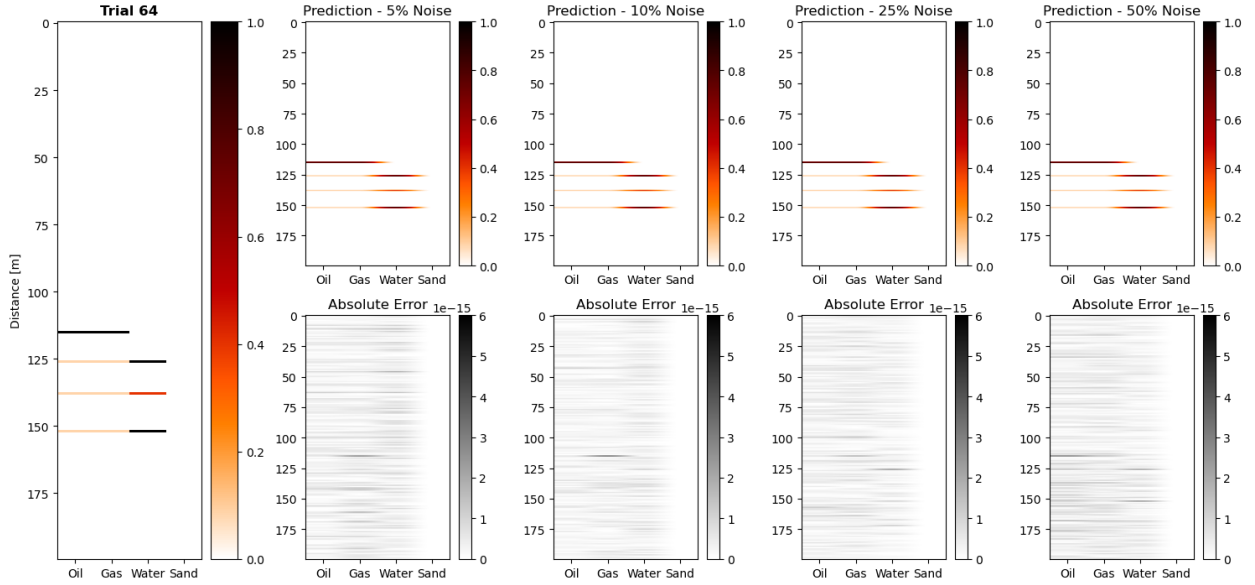


**Figure 18:** Prediction of physical flow properties for Trial 64 with different levels of added noise; (A) is the true relative rates, (B) 5% noise, (C) 10% noise, (D) 25% noise, and (E) 50% noise. The top row shows the estimated physical flow properties, and the bottom row shows the absolute error.

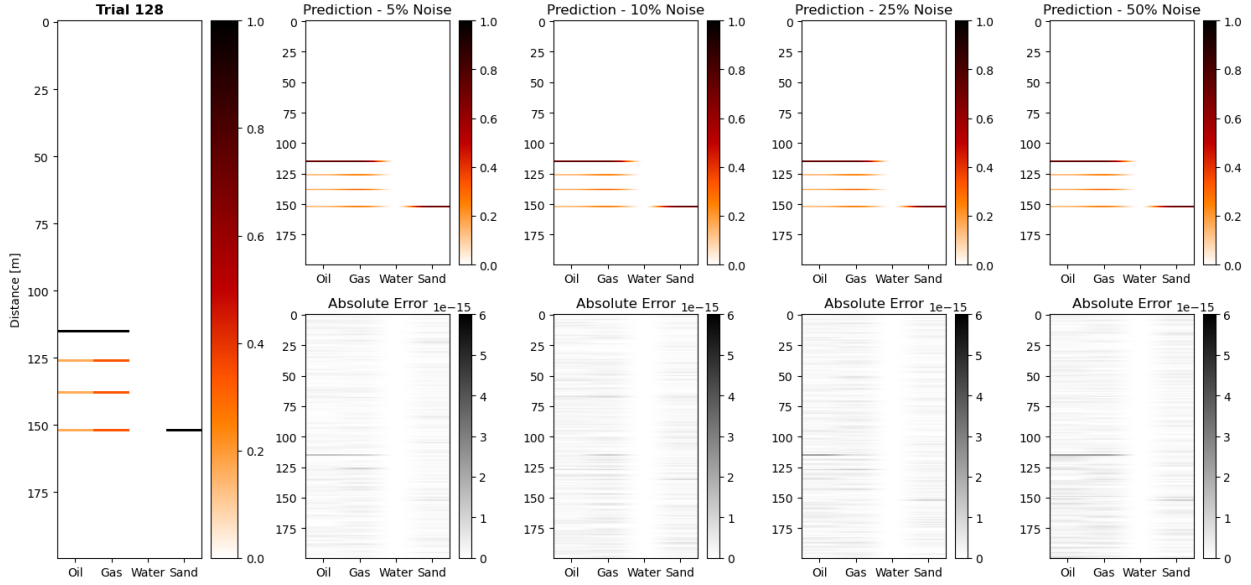


**Figure 19:** Prediction of physical flow properties for Trial 128 with different levels of added noise; (A) is the true relative rates, (B) 5% noise, (C) 10% noise, (D) 25% noise, and (E) 50% noise. The top row shows the estimated physical flow properties, and the bottom row shows the absolute error.

### 226 3.5 Discussion

227 Our proposed dual latent space model provides accurate and computationally efficient predictions of physical  
 228 flow properties from DFOS measurements. The proposed method is capable of estimating the injection  
 229 point location and relative multiphase flow rates within 7-9 significant figures, in under 10 milliseconds.  
 230 The entire workflow, including the data processing, resampling, model training, and property prediction,  
 231 takes approximately 4.44 seconds on an Intel i9-10900K CPU. This provides an opportunity for real time  
 232 monitoring using DFOS measurements with frequent re-processing and re-training to continuously improve  
 233 model performance.

234 Comparing the single latent space models to the dual latent space model, we observe a slight advantage  
 235 when combining both DAS and DTS data into the estimation of the physical flow properties. However, given  
 236 that the estimation problem is highly over-determined, a single latent space model could still be useful for a  
 237 wide array of applications. The difference in terms of accuracy is between 1 and 2 orders of magnitude, yet  
 238 still very small, in the order of  $10^{-7}$ - $10^{-9}$ . Furthermore, there is no noticeable computational savings when  
 239 using a single or dual latent space model, given that the DAS and DTS Encoders are both pre-trained and  
 240 provide the latent representations in less than 10 milliseconds.

241 Moreover, the dual latent space model shows robustness to noise. Given that DAS and DTS measurements  
 242 are very noisy in nature, adding further noise does not affect significantly the accuracy of the predictions.

243 The Encoder networks show robustness to noise, and are still capable of extracting the salient latent features  
244 in the DAS and DTS measurements despite increasing levels of noise. This is promising due to the fact  
245 that our dual latent space model is trained with measurements from a controlled flow-loop experiment and  
246 subsurface applications are more likely to include higher noise levels.

## 247 4 Conclusions

248 We present a novel deep learning-based architecture for the prediction of injection points and relative rates  
249 based on distributed fiber optic sensing measurements. The proposed methodology exploits the spatiotempo-  
250 ral latent space from time-lapse DAS and DTS measurements through a double-U-Net architecture. Measure-  
251 ments from controlled flow-loop experiments with multiphase flow are used to train the network and extract  
252 acoustic and temperature latent spaces. These are combined in order to accurately predict the points of  
253 injection along the flow-loop as well as the relative rates of each phase passing through the perforations.

254 The double-U-Net architecture is designed in a modular fashion, with one convolutional U-net AutoEn-  
255 coder for the time-lapse DAS data and a separate convolutional U-net AutoEncoder for the time-lapse DTS  
256 data. However, both AutoEncoders are exactly the same in terms of architecture but trained separately due  
257 to the difference in sampling rate of the two signals. The AutoEncoders are designed with four convolutional  
258 blocks encoding the data into a latent space and four transpose convolutional blocks, which are concatenated  
259 to the original encoder blocks using residual concatenations, onto the decoded time-lapse signal. The pa-  
260 rameters are trained to minimize the difference between the original and reconstructed signals. The Encoder  
261 portions of the two architecture are extracted and used to generate the acoustic and temperature latent  
262 spaces, respectively. A third estimator is designed to receive the combined latent space and predict a mask  
263 containing the injection locations and relative rates.

264 The entire training process required approximately 27 minutes on a single NVIDIA Quadro M6000 GPU.  
265 Training is done with one experimental dataset, and testing is performed with different experimental data.  
266 Errors are consistently below  $3.68 \times 10^{-9}\%$  and signal similarity is over 98.9%. After the pre-training is  
267 done, predictions of physical flow properties are obtained in under 10 milliseconds.

268 Therefore, this model can be used for real-time predictions and evaluation of subsurface energy systems  
269 in applications such as oil and gas production, hydraulic fracturing monitoring, geologic carbon storage,  
270 and geothermal energy production. To our knowledge, our work is the first to develop a methodology  
271 for reduced-dimensional modeling of distributed fiber optic sensing data, and the prediction of injection  
272 locations and relative rates through the enhanced latent space for accurate and real-time multiphase fluid  
273 flow characterization. Future opportunities include varying the number and location of the injection points to

274 generate more training samples, applying a transfer learning protocol to predict the physical flow properties  
275 on other subsurface scenarios (e.g., enhanced oil recovery, CO<sub>2</sub> sequestration), and deploying the model on  
276 the cloud for real-time processing instead of post-processing.

## 277 **Reproducibility**

278 The code will be made publicly available on the author's repository ([github.com/misaelmmorales](https://github.com/misaelmmorales)).

## 279 **Funding**

280 This research did not receive any specific grant from funding agencies in the public, or not-for-profit sectors.

## 281 **Declarations**

282 The authors declare no conflict of interests.

## 283 **Acknowledgements**

284 The authors thank the Formation Evaluation (FE) and Digital Reservoir Characterization Technology (DI-  
285 RECT) Industry Affiliate Programs at the University of Texas at Austin for supporting this work.

## 286 **References**

- 287 [1] Bin Luo, Ariel Lellouch, Ge Jin, Biondo Biondi, and James Simmons. Seismic inversion of shale reservoir properties using microseismic-induced guided waves recorded by distributed acoustic sensing. *Geophysics*, 86(4):R383–R397, 2021.
- 288  
289
- 290 [2] Fuad Aziz Atakishiyev, Alessandro Delfino, Cagri Cerrahoglu, Zahid Hasanov, Ilkin Yusifov, Alex Wallace, and Alberto Mendoza. Flow Diagnostics in High Rate Gas Condensate Well Using Distributed Fiber-Optic Sensing and its Validation with Conventional Production Log. volume Day 1 Tue, September 07, 2021 of *SPE Offshore Europe Conference and Exhibition*, page D011S002R002, 09 2021. doi: 10.2118/205435-MS.
- 291  
292  
293  
294
- 295 [3] Abhishek Venketeswaran, Nageswara Lalam, Jeffrey Wuenschell, Paul R Ohodnicki Jr, Mudabbir Badar,

- 296 Kevin P Chen, Ping Lu, Yuhua Duan, Benjamin Chorpening, and Michael Buric. Recent advances in  
297 machine learning for fiber optic sensor applications. *Advanced Intelligent Systems*, 4(1):2100067, 2022.
- 298 [4] A Mateeva, J Lopez, D Chalenski, M Tatanova, P Zwartjes, Z Yang, S Bakku, K de Vos, and H Potters.  
299 4d das vsp as a tool for frequent seismic monitoring in deep water. *The Leading Edge*, 36(12):995–1000,  
300 2017.
- 301 [5] Paul Zwartjes, Albena Mateeva, David Chalenski, Yuting Duan, Denis Kiyashchenko, and Jorge Lopez.  
302 Frequent, multi-well, stand-alone 3d das vsp for low-cost reservoir monitoring in deepwater. In *SEG  
303 Technical Program Expanded Abstracts 2018*, pages 4948–4952. Society of Exploration Geophysicists,  
304 2018.
- 305 [6] Zahid Hasanov, Parviz Allahverdiyev, Fuad Ibrahimov, Alberto Mendoza, Pradyumna Thiru-  
306 venkatanathan, Lilia Noble, and Jonathan Stapley. Production Optimization of Sanding Horizontal  
307 Wells Using a Distributed Acoustic Sensing (DAS) Sand Monitoring System: A Case Study From the  
308 ACG Field in Azerbaijan. volume Day 1 Mon, May 17, 2021 of *SPWLA Annual Logging Symposium*,  
309 page D011S001R001, 05 2021. doi: 10.30632/SPWLA-2021-0001.
- 310 [7] Rolf Birger Pedersen, LJ Reigstad, and T Baumberger. Cruise report gs12a-scientific cruise to the  
311 sleipner area in the north sea; r/v go sars expedition no. 2012108/cgb2012, june 22th-30th 2012, bergen,  
312 norway-bergen, norway. 2012.
- 313 [8] Islam Ashry, Yuan Mao, Biwei Wang, Frode Hveding, Ahmed Y Bukhamsin, Tien Khee Ng, and Boon S  
314 Ooi. A review of distributed fiber-optic sensing in the oil and gas industry. *Journal of Lightwave  
315 Technology*, 40(5):1407–1431, 2022.
- 316 [9] Daniele Inaudi and Branko Glisic. Fiber optic sensing for innovative oil & gas production and transport  
317 systems. In *Optical Fiber Sensors*, page FB3. Optica Publishing Group, 2006.
- 318 [10] Thomas M Daley, Barry M Freifeld, Jonathan Ajo-Franklin, Shan Dou, Roman Pevzner, Valeriya Shu-  
319 lakova, Sudhendu Kashikar, Douglas E Miller, Julia Goetz, Jan Henniges, et al. Field testing of  
320 fiber-optic distributed acoustic sensing (das) for subsurface seismic monitoring. *The Leading Edge*, 32  
321 (6):699–706, 2013.
- 322 [11] Derrick Chambers, Ge Jin, Ahmad Tourei, Abdul Hafiz Saeed Issah, Ariel Lellouch, Eileen Martin,  
323 Donglin Zhu, Aaron Girard, Shihao Yuan, Thomas Cullison, et al. Dascore: a python library for  
324 distributed fiber optic sensing. 2024.

- 325 [12] Hasan Asy'ari Arief, Tomasz Wiktorski, and Peter James Thomas. A survey on distributed fibre optic  
326 sensor data modelling techniques and machine learning algorithms for multiphase fluid flow estimation.  
327 *Sensors*, 21(8):2801, 2021.
- 328 [13] CS Sherman, RJ Mellors, and JP Morris. Subsurface monitoring via physics-informed deep neural  
329 network analysis of das. In *ARMA US Rock Mechanics/Geomechanics Symposium*, pages ARMA–2019.  
330 ARMA, 2019.
- 331 [14] Vincent Dumont, Verónica Rodríguez Tribaldos, Jonathan Ajo-Franklin, and Kesheng Wu. Deep learning  
332 for surface wave identification in distributed acoustic sensing data. In *2020 ieee international  
333 conference on big data (big data)*, pages 1293–1300. IEEE, 2020.
- 334 [15] Steven L Brunton, Joshua L Proctor, and J Nathan Kutz. Discovering governing equations from data by  
335 sparse identification of nonlinear dynamical systems. *Proceedings of the national academy of sciences*,  
336 113(15):3932–3937, 2016.
- 337 [16] William D Fries, Xiaolong He, and Youngsoo Choi. Lasdi: Parametric latent space dynamics identifi-  
338 cation. *Computer Methods in Applied Mechanics and Engineering*, 399:115436, 2022.
- 339 [17] Vincent Dumont, Verónica Rodríguez Tribaldos, Jonathan Ajo-Franklin, and Kesheng Wu. Deep learn-  
340 ing on real geophysical data: A case study for distributed acoustic sensing research. *arXiv preprint  
341 arXiv:2010.07842*, 2020.
- 342 [18] Yankun Sun, Jinquan Liu, Ziqiu Xue, Qi Li, Chengkai Fan, and Xu Zhang. A critical review of dis-  
343 tributed fiber optic sensing for real-time monitoring geologic co2 sequestration. *Journal of Natural Gas  
344 Science and Engineering*, 88:103751, 2021.
- 345 [19] Teymur Sadigov, Cagri Cerrahoglu, James Ramsay, Laurence Burchell, Sean Cavalero, Thomas Wat-  
346 son, Pradyumna Thiruvenkatanathan, and Martin Sundin. Real-time water injection monitoring with  
347 distributed fiber optics using physics-informed machine learning. In *Offshore Technology Conference*,  
348 page D041S054R007. OTC, 2021.
- 349 [20] Shuvajit Bhattacharya, Payam Kavousi Ghahfarokhi, Timothy R Carr, and Scott Pantaleone. Ap-  
350 plication of predictive data analytics to model daily hydrocarbon production using petrophysical, ge-  
351 omechanical, fiber-optic, completions, and surface data: A case study from the marcellus shale, north  
352 america. *Journal of Petroleum Science and Engineering*, 176:702–715, 2019.
- 353 [21] Zhaoqiang Peng, Jianan Jian, Hongqiao Wen, Andrei Gribok, Mohan Wang, Hu Liu, Sheng Huang,  
354 Zhi-Hong Mao, and Kevin P Chen. Distributed fiber sensor and machine learning data analytics for

- 355 pipeline protection against extrinsic intrusions and intrinsic corosions. *Optics Express*, 28(19):27277–  
356 27292, 2020.
- 357 [22] King Ma, Henry Leung, Ehsan Jalilian, and Daniel Huang. Fiber-optic acoustic-based disturbance  
358 prediction in pipelines using deep learning. *IEEE Sensors Letters*, 1(6):1–4, 2017.
- 359 [23] Fantine Huot, Ariel Lellouch, Paige Given, Bin Luo, Robert G Clapp, Tamas Nemeth, Kurt T Nihei,  
360 and Biondo L Biondi. Detection and characterization of microseismic events from fiber-optic das data  
361 using deep learning. *Seismological Society of America*, 93(5):2543–2553, 2022.
- 362 [24] Alberto Mendoza, Çagri Cerrahoglu, Alessandro Delfino, and Martin Sundin. Signal processing and ma-  
363 chine learning for effective integration of distributed fiber optic sensing data in production petrophysics.  
364 In *SPWLA Annual Logging Symposium*, page D031S003R006. SPWLA, 2022.
- 365 [25] *Downhole Sand Ingress Detection Using Fibre-Optic Distributed Acoustic Sensors*, volume Day 3 Wed,  
366 November 09, 2016 of *Abu Dhabi International Petroleum Exhibition and Conference*, 11 2016. doi:  
367 10.2118/183329-MS.
- 368 [26] MD McKay and WJ Conover. Rj beckman a comparison of three methods for selecting values of input  
369 variables in the analysis of output from a computer code. *Technometrics*, 21:239–245, 1979.
- 370 [27] Olaf Ronneberger, Philipp Fischer, and Thomas Brox. U-net: Convolutional networks for biomedical  
371 image segmentation. In *Medical Image Computing and Computer-Assisted Intervention–MICCAI 2015:*  
372 *18th International Conference, Munich, Germany, October 5-9, 2015, Proceedings, Part III* 18, pages  
373 234–241. Springer, 2015.
- 374 [28] Diederik P Kingma and Jimmy Ba. Adam: A method for stochastic optimization. *arXiv preprint  
375 arXiv:1412.6980*, 2014.
- 376 [29] Zhou Wang, Alan C Bovik, Hamid R Sheikh, and Eero P Simoncelli. Image quality assessment: from  
377 error visibility to structural similarity. *IEEE transactions on image processing*, 13(4):600–612, 2004.